CONFERENCE PRE-PRINT

IMPACT OF RADIATION DISTRIBUTION ON DETACHMENT ONSET AND IMPLICATIONS FOR STEP DIVERTOR DESIGN

M. Kryjak
United Kingdom Atomic Energy Authority
Abingdon, United Kingdom of Great Britain and Northern Ireland
Email: mike.kryjak@ukaea.uk

C. Cowley
digiLab
Exeter, United Kingdom of Great Britain and Northern Ireland

D. Moulton, S. S. Henderson, R. T. Osawa, O. Myatra
United Kingdom Atomic Energy Authority
Abingdon, United Kingdom of Great Britain and Northern Ireland

B. D. Dudson
Lawrence Livermore National Laboratory
Livermore, United States of America

P. Hill, L. Pattinson, C. Ridgers
York Plasma Institute, Department of Physics, University of York
York, United Kingdom of Great Britain and Northern Ireland

Abstract

Reactor-class devices such as STEP feature high divertor heat fluxes requiring detachment for an acceptable exhaust solution. Detachment in high-power devices is only possible through seeded impurity radiation, which then dominates the energy losses. This fact is exploited by the DLS (Detachment Location Sensitivity) analytical 0.5D model, which can predict the impact of divertor magnetic geometry on detachment access and front movement sensitivity and perform rapid divertor design scoping studies. This paper introduces DLS-Extended, a 1D version of the DLS which additionally predicts the distribution of the radiation instead of assuming it to be infinitely thin. This allows the radiation effects to be isolated and studied in detail to find their impact on divertor design optimisation. Existing SOLPS-ITER simulations of an interim STEP design show that the impurity radiation extends throughout the divertor leg for both the inner and outer targets, with DLS-Extended matching the distribution well in flux tubes without significant cross-field transport. This broad radiation is found to interact with the magnetic geometry of the divertor through several novel effects. The effect of B field variation is reduced and connection length variation is increased, leading to a different optimal strike point position for both divertors. There is a substantial improvement in detachment front stability for the inner, and a small decrease in front stability for the outer divertor. The results show that both divertors are less sensitive to the horizontal strike-point position with increasing radiation width, and that the inner divertor detachment access can be substantially improved by lowering the strike-point.

1. INTRODUCTION

One of the most pressing issues for reactor-relevant tokamaks is the core-edge compatibility challenge [1] where reactor-scale tokamaks are predicted to produce unmitigated divertor heat loads higher than what known materials can withstand [2, 3]. The most promising solution currently lies in detachment, where the divertor target is protected by the detached region - a cloud of cool neutral gas which prevents direct plasma contact with solid material.

In the detached regime, a high power, high-temperature, conduction-dominated plasma terminates at the interface between the plasma and neutral regions, which is commonly referred to as the detachment front [4]. High-power, reactor-class devices such as the United Kingdom STEP spherical tokamak [5] require admission

of impurity species such as nitrogen, argon or neon to increase radiation and access detachment [6]. This radiation then dominates the energy losses, a fact used by a class of reduced models based on the Lengyel model [7, 8, 9, 10], including the DLS (Detachment Location Sensitivity) model [11, 4, 12]. The DLS is a simple analytical model able to capture the impact of divertor magnetic geometry on detachment access and sensitivity, enabling quick scoping studies during early-stage divertor design.

The effects of magnetic geometry on detachment have been studied in several devices, including TCV [13, 14, 15, 16], DIII-D [17, 18, 19] and MAST-U [20, 21] as well as in simulations [4, 22, 23, 24], but very few studies included the impact of impurity radiation. The DLS model assumes that the radiation region is infinitely thin, which was proven invalid in a recent study comparing DLS to MAST-U simulations with impurity transport [12] which found that the radiation extended throughout the divertor even with nitrogen seeding, an impurity often considered to be "narrow-radiating". Since STEP uses argon, a broader-radiating impurity, this finding motivates the need to investigate the role of radiation distribution in divertor design by using the first-principles framework of the DLS model.

In this work, we relax the thin radiation assumption of the original 0.5D model (hereon named DLS-Simple) and introduce DLS-Extended - a new, fast reduced 1D model which self-consistently solves the spatial profiles of heat flux and impurity radiation. We perform a baseline verification of the impurity distribution against SOLPS-ITER [25] simulations of an intermediate STEP design [26]. Using this solution as the baseline, we find that a spatially broad radiation region can lead to significant changes in the benefit of f_R and $L_\parallel$ on detachment access and sensitivity for both the inner and outer divertors, leading to a different optimum strike point position for the inner and outer divertors.

2. DLS-EXTENDED

The original DLS model was first derived in [11], and then re-derived for a simpler coordinate system while omitting the upstream region in [4]. It considers two points - the upstream and the front - and performs an energy balance between the input and radiated power to find conditions required for the detachment front to be in a particular location. In this work, we build on preliminary work in [27] and introduce the new model DLS-Extended which relaxes the infinitely thin radiation front assumption. This is achieved by repeating the DLS-Simple derivation [4] without taking the assumption and solving the two resulting ODEs numerically at very low computational cost. We start with the energy balance equation cast in its continuous form:

$$B\frac{d}{ds}\left(\frac{q_{||}}{B}\right) = n^2 f_\alpha L_\alpha(T) - Q_{in}, \tag{1}$$

Where B is the total B field, $q_\parallel$ the electron parallel heat flux, n the electron density, f_α the fraction of impurity species α, $L_\alpha(T)$ the cooling function of the impurity species with respect to temperature and Q_{in} the uniform energy source term corresponding to cross-field heat transport between the upstream and the X-point. In the present work, the upstream is always defined as the midplane. Q_{in} is calculated from a user input of unmitigated X-point heat flux $q_{\parallel,X0}$:

$$Q_{in} = \frac{q_{\parallel,X0}}{B_X \int_{s_{\parallel,X}}^{s_{\parallel,u}} \frac{1}{B} ds_\parallel}. \tag{2}$$

The electron density is determined by assuming a constant electron static pressure throughout the field line, so that $n = \frac{n_u T_u}{T}$. This allows equation 1 to be rearranged in terms of the temperature along the field line, which becomes the first DLS-Extended equation:

$$B\frac{d}{ds}\left(\frac{q_{||}}{B}\right) = \frac{n_u^2 T_u^2}{T^2} f_\alpha L_\alpha(T) - Q_{in}. \tag{3}$$

The second equation is the temperature along the field line obtained by rearranging the Spitzer-Härm model [28]:

$$\frac{dT}{ds} = \frac{q_\parallel}{\kappa_{e0} T^{5/2}}. \tag{4}$$

Both ODEs are numerically integrated from the detachment front to the midplane, and a binary search algorithm finds the upstream density, power or impurity fraction required for the front to be in the requested position. This is initially done with an estimate of T_u and repeated with calculated T_u until convergence (similar to [10]). The model needs the following inputs:

- A parallel profile of the total B field
- $L_\alpha(T)$, the electron cooling function of impurity α

- κ_{e0}, the Spitzer electron conductivity divided by $T^{5/2}$
- Any two of n_u, f_α or Q_{in}
- The front location

The conditions at the detachment front are input as boundary conditions: T_e and $q_\parallel$, which both must be non-zero for numerical reasons ($T_e = 0.5eV$ and $q_{\parallel,f}$ being 5% of the unmitigated heat flux at the X-point in the present work). The model outputs are the 1D profiles of electron density, temperature, parallel heat flux and radiated power as well as the value of the chosen control outputs (any two of n_u, f_α or Q_{in}). DLS-Extended is publicly available on GitHub [29] under the LGPL-3 open source license. The repository includes example Jupyter notebooks which also serve as continuous integration tests.

3. COMPARISON TO SOLPS-ITER

In order to verify the DLS-Extended predictions of radiation distribution, the results were compared to SOLPS-ITER simulations of STEP based on an initial design iteration [26]. Out of the configurations studied in that work, the midplane puff was chosen for the comparison due to a more constant plasma pressure along the divertor leg compared to the other configurations. The simulations included impurity transport and currents, but neglected drifts were neglected for simplicity while keeping the parallel closure choice at the version 3.0.8 default. The conditions included a P_{sep} of 100 MW in a detached, connected double null configuration. The fuelling is primarily achieved at the midplanes, argon is admitted through a puff in each of the divertor legs and the neutral pump is located on the outer wall of the outer divertor leg.

The comparison to DLS-Extended results requires care due to the number of simplifications compared to SOLPS. Since advection, cross-field transport and neutral physics are entirely neglected, electron pressure is assumed to be conserved along the field line. This results in density increasing inversely proportionately to temperature, which itself is controlled by impurity radiation and electron conduction only. The impact of conduction flux limiters is neglected with κ_{e0} kept constant. While SOLPS solves the transport and radiation of each argon charge state, DLS-Extended includes impurity radiation through the fixed-fraction model, where impurity density is a constant fraction of electron density and the radiation is computed from a "cooling curve" which is a function of temperature and assumes a fixed charge state distribution. This means that DLS-Extended does not account for local variations in impurity density and the results are be sensitive to cooling curve choice.
The model front is defined by $T_e = 0.5eV$ and $q_{\parallel,f}$ being 5% of the unmitigated heat flux at the X-point. These conditions must be non-zero for numerical reasons and were arbitrarily chosen to provide a better qualitative match to the SOLPS-ITER simulations in section 3, and their absolute value has no impact on the results of the present study.

A baseline DLS-Extended simulation was performed on both the inner and outer divertor. The third SOL ring was chosen in each case to strike a balance between the relevance of the flux tube in determining detachment conditions and model validity: maximising the parallel heat flux and minimising the role of cross-field transport and convective heat transfer. The power source was chosen such that the total X-point parallel heat flux in SOLPS matches the total (electron) parallel heat flux in DLS-Extended. The front location and upstream density are user inputs and were set to be the same as SOLPS, with the DLS front boundary conditions chosen as the point where $T_e = 5eV$ 95% of the unmitigated upstream heat flux has been mitigated. The precise boundary condition value has no impact on the conclusions of the present study. The impurity radiation cooling curve was set to be the same as SOLPS by extracting it from the chosen SOL ring:

$$L_{Ar}^{SOLPS} = \frac{Q_{rad,Ar}}{n_e^2 f_{Ar}}. \tag{5}$$

While it is possible to also extract an "effective" electron conductivity from SOLPS (see [8]), the value would be affected by several mechanisms not present in DLS-Extended - the conductivity can vary due to frictional effects and flux limitation, and the heat flux profiles can be significantly affected by the presence of convection, reactions and cross-field transport. Because of this, any back-calculated conductivity value would not be physically meaningful in the DLS and act as a tuning parameter. Therefore, the comparison is first performed using the DLS-Extended default value $\kappa_{0,e} = 2500Wm^{-1}eV^{-7/2}$, and then using a value tuned qualitatively to obtain a better temperature profile match. This required a very small adjustment for the outer and a very large adjustment for the inner: 2250 $\mathrm{Wm^{-1}eV^{-7/2}}$ and 6400 $\mathrm{Wm^{-1}eV^{-7/2}}$, respectively. The value for the inner is unrealistically high due to the fact it compensates by a substantial amount of upstream convective heat flux driven by the midplane puff.

The model outputs are the profiles of radiation, temperature and heat flux, as well as the absolute value of the constant impurity fraction required for the front to be at the requested position. As this work focuses on scalings and not absolute predictions, the assessment of the accuracy of the impurity fraction prediction is beyond the scope; see [8, 9] and especially [30] for detailed studies of the absolute accuracy of Lengyel-based models. The results of the comparison are shown in fig. 1. The SOLPS simulations predict that the impurity radiation is spread over a large region in both divertors, confirming that the infinitely thin radiation region assumption is invalid in this case.

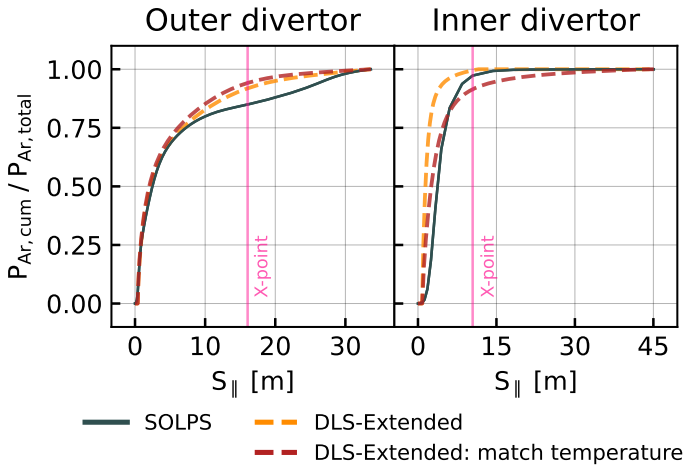

FIG. 1. A comparison of the DLS-Extended and SOLPS-ITER radiation distributions for the 3rd SOL ring in the inner and outer divertor shown through a cumulative integral of $P_{rad,ar}$. The x-axis shows parallel distance from target.

DLS-Extended matches the SOLPS radiation distribution well for the chosen SOL ring in each of the divertors, but with the inner divertor relying on tuning the conductivity to match the temperature profile due to its high upstream convection. The main discrepancy in the outer divertor is the broader radiation around the X-point seen in SOLPS; this is caused by cross-field transport driving local density changes affecting radiative power. A detailed comparison was performed for other SOL rings which were less favourable to the comparison (not shown). It was found that the radiation distribution predictions hold up well even in the presence of significant convective flows, but the match in SOL rings near the separatrix was strongly impacted by the argon puff enhancing local radiative power. The results were also found to be sensitive to the cooling curve choice. Overall, it was found that the radiation region has a broad extent over all key SOL rings in the inner and outer divertors, and that DLS-Extended performs well in predicting the radiation region extent.

4. IMPACT OF RADIATION DISTRIBUTION ON DETACHMENT

4.1. Detachment performance metrics

In the previous DLS-Simple work [4], upstream conditions are lumped into a control variable C and an analytical expression for how C at detachment threshold depends on magnetic geometry, including total flux expansion and connection length which are two key parameters in many advanced divertor configurations. However, the novel radiation effects in DLS-Extended add complex, nonlinear behaviour. Because of this, we choose a more general expression:

$$\left.\frac{n_u\sqrt{f_\alpha}}{Q_{in}^{5/7}}\right|_{threshold} \propto \left[L_\parallel\right]^{-K_{L_\parallel}} \left[f_R\right]^{-K_{f_R}}. \tag{6}$$

Here we define f_R as the ratio of B at the X-point to that at the target, and $L_\parallel$ as the total parallel connection length between the midplane and the target. The coefficients K_{f_R} and $K_{L_\parallel}$ increase the sensitivity of detachment threshold to the relevant leg geometry quantity. In the narrow radiation limit, two-point model based analysis of DLS-Simple, these proportionalities reduce to analytically derived values of approx. 1 and $2/7$ for K_{f_R} and $K_{L_\parallel}$, respectively, which are hereon referred to as "classical" scalings which are also present in the modified two-point model [18]. However, the factors are not constant in reality.

$K_{f_R} \approx 1$ originates from total flux expansion increasing the flux tube area, diluting $q_\parallel$ and easing detachment. It has been reproduced in dedicated slab geometry SOLPS simulations [4] featuring a narrow nitrogen cooling curve, as well as in unseeded experiments at DIII-D [18]. A strong impact was also found in unseeded MAST-U shots [21]. TCV experiments and simulations found that the effect can be mitigated, or even reversed depending on the neutral closure [13, 31, 15], suggesting that tightly baffled designs are required to maximise the effect. A recent study also found a potential enhancement through SOL broadening effects [19]. To the authors' best knowledge, no work has yet analysed K_{f_R} in broad-radiating conditions.

$K_{L_\parallel} = 2/7 = 0.29$ originates from the two-point model / Spitzer-Härm [28] conduction expression, where extra flux tube length leads to a higher T_u for a cold, constant T_f, leading to higher n_t due to $n_u T_u = n_f T_f$. It is ubiquitous among two-point model implementations [32, 10, 33, 11] but first-principles enhancement mechanisms from have not been studied as widely. Two enhancement mechanisms present in DLS-Extended have been reported previously: a stronger scaling if L_{div} is changed instead of $L_\parallel$ through its different impact on $\int_f^u q_\parallel ds_\parallel$ in [11] and a stronger scaling in broad radiation in [10] finding $K_{L_\parallel} = 0.43$ which was later partially empirically reproduced in the Kallenbach detachment qualifier model [23]. The enhancement is present if impurity radiation extends to the midplane, resulting in more radiating volume at greater $L_\parallel$. This manifests as an increased Lengyel integral term, as discussed in the following section. Other studies found an enhanced $K_{L_\parallel} \approx 0.60$ through SOL broadening [16] and pressure loss-related effects [4], although neither has been conclusively explained yet.

In section 4.2 we show that in addition to the effects found above, K_{f_R} and $K_{L_\parallel}$ are strongly modified in the presence of broad impurity radiation. We also study the impact on the detachment window, which is a crude measure of detachment front sensitivity, defined as $W = \frac{A_X}{A_t}$ where A represents the front-controlling variable n_u, f_α or Q_{in}. The detachment window W represents the range of the chosen variable to span the detachment operational space (between detachment threshold and X-point radiator). Regions where $W < 1$ are unstable - the detachment is easier to achieve at the X-point than at the target, leading to detachment cliff-like behaviour. This can be caused by flux compression.

4.2. Quantifying radiation impact

In order to quantify the impact of the radiation distribution on the effectiveness of f_R and $L_\parallel$, the baseline DLS-Extended result was compared to one with double the total flux expansion and double the connection length. The magnetic geometry was changed only below the X-point through the modification of the total B field profile DLS-Extended input. For simplicity, density was chosen as the outputted upstream condition, and so K_{f_R} and $K_{L_\parallel}$ can be obtained by comparing the upstream density required for detachment threshold in each case to the change in the relevant magnetic geometry quantity, as according to equation 6.

This procedure was repeated for a number of cooling curves in order of increasing width: an arbitrary analytical thin curve, argon in the coronal approximation, non-coronal argon and non-coronal neon. The argon and neon curves were generated using the open-source tool radas [34] based on OpenADAS data, with the non-coronal argon and neon set to $n_e\tau = 5 \times 10^{-19}\mathrm{m}^{-3}\mathrm{ms}$ as per [8], which was found to give reasonable agreement with the SOLPS-extracted cooling curve. The SOLPS curve is omitted for this study due to being invalid when T_u exceeds that in the original simulation. To understand the resulting effects in more detail, the DLS-Extended equations were derived in an analytical form:

$$\frac{\sqrt{f_\alpha} n_u}{Q_{in}^{5/7}} = B_{eff} \frac{Q_{in}^{2/7}}{T_u} \frac{\sqrt{2\int_{s_X}^{s_u} \frac{q_{||}}{Q_{in} B^2} ds_\parallel}}{\sqrt{2\int_{T_f}^{T_u} \kappa_{e0} T^{1/2} L_\alpha(T) dT}}, \tag{7}$$

Where B_{eff} is the radiation-averaged magnetic field:

$$B_{eff} = \sqrt{\frac{\int_{s_f}^{s_u} q_\parallel Q_{rad} ds_\parallel}{\int_{s_f}^{s_u} q_\parallel Q_{rad}/B^2 ds_\parallel}} = \frac{\sqrt{2\int_{T_f}^{T_u} \kappa_{e0} T^{1/2} L_\alpha(T) dT}}{\sqrt{2\int_{T_f}^{T_u} \frac{\kappa_{e0} T^{1/2} L_\alpha(T)}{B^2} dT}}. \tag{8}$$

Each term in equation 7 is assigned a symbol such that $\frac{\sqrt{f_\alpha} n_u}{Q_{in}^{5/7}} = \alpha\beta\gamma\delta$, where α corresponds to B_{eff}, representing total flux expansion effects, β to $\frac{Q_{in}^{2/7}}{T_u}$ which represents heat flux profile changes that would modify T_u as in the classical $L_\parallel$ scaling, γ to $\left(\sqrt{2\int_{T_f}^{T_u} \kappa_{e0} T^{1/2} L_\alpha(T) dT}\right)^{-1}$, representing changes to the Lengyel (radiation) integral and finally δ which corresponds to the term $\sqrt{2\int_X^u \frac{q_{||}}{Q_{in} B^2} ds_\parallel}$ and represents the impact of upstream radiation. In this way, we decompose each scaling factor into individual components, e.g. $K_{f_R} = K_{f_{R,\alpha}} + K_{f_{R,\beta}} + K_{f_{R,\gamma}} + K_{f_{R,\delta}}$, with the results shown in figure 2.

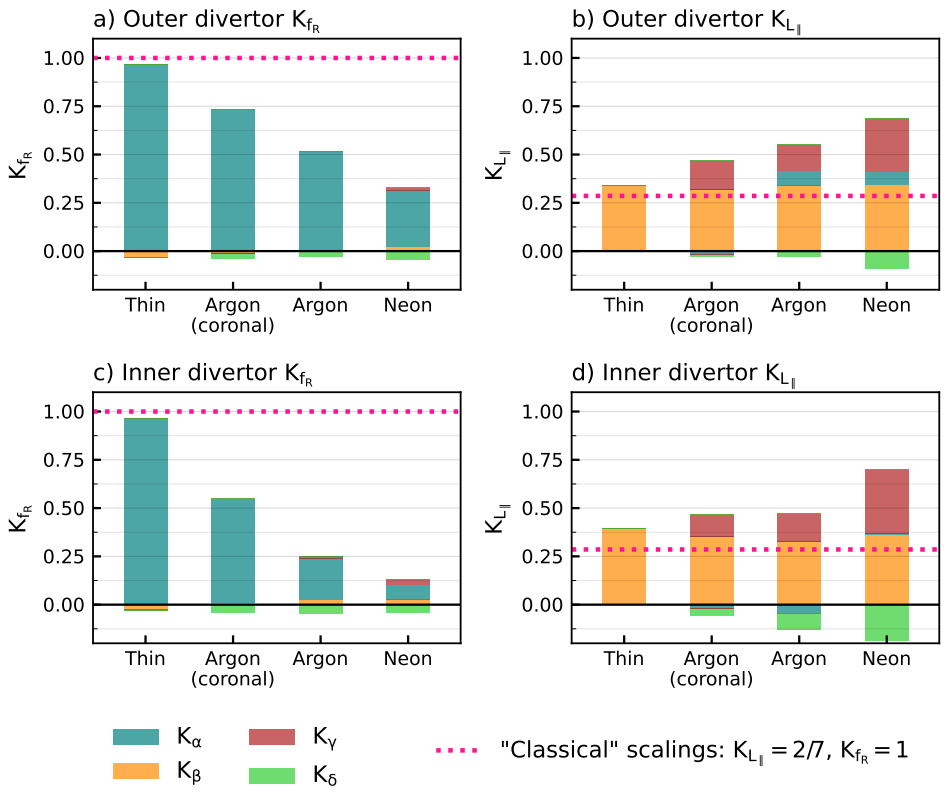

FIG. 2. Detachment access scalings K_{f_R} (left) and $K_{L_\parallel}$ (right) for each cooling curve for the outer (top) and lower (bottom) divertor, broken down by term contribution, along with simple analytical scaling factors.

It can be seen that the thin curve already departs from the classical scalings even without any radiation effects. In the case of f_R, this is because the $q_\parallel$ integral is slightly modified when changing total flux expansion, changing T_u and so manifesting through a small negative term β. In the case of $L_\parallel$, DLS-Extended features a higher average $q_\parallel$ in the divertor, causing changes in L_{div} having a greater impact than $L_\parallel$.

The most striking effect seen in figure 2 is the dramatic reduction of K_{f_R} as radiation broadens. This is due to broad radiation "averaging out" the B-field in each case, and therefore reducing the impact of increasing f_R. This can be represented through an effective reduction in f_R, defined as $f_{R,eff} = \frac{B_X}{B_{eff,target}}$. As the radiation region narrows, $B_{eff,target} \rightarrow B_{target}$ and $f_{R,eff} \rightarrow f_R$. As it broadens, $B_{eff,target} \rightarrow \bar{B}$. This averaging effect is illustrated in figure 3a and can be slightly mitigated if the upstream radiation increases (figure 3b). These are particularly strong effects for the inner whose divertor region is a smaller proportion of the total connection length, allowing radiation to span the entire leg more easily as shown by the dramatically reduced K_{f_R} in figure 2. The effect also interacts with connection length, as shown in figure 3c. Increasing $L_\parallel$ reduces the radiation width as a proportion of the field line: the connection length increases, but the radiation region narrows due to the resulting slightly steeper temperature gradient. This partially reverses the mechanism shown in 3a, bringing $f_{R,eff}$ closer to f_R. This effect is responsible for the role of term α in the connection length results in figure 2.

The term β varies only slightly: it's affected by any changes in the $q_\parallel$ integral, which are brought on by f_R and radiation effects. Term γ represents the Lengyel integral - the domain integral of the cooling curve to obtain the total radiation. This term is usually assumed to be constant for a given cooling curve, e.g. in [8], [4]. This is not the case in broad radiation, as first described in [10], and the impact of this is captured by term γ being non-zero. If the curve allows additional radiation beyond T_u, then increasing $L_\parallel$ will increase total radiative losses as T_u increases. Said another way, if there is already radiation at the high-temperature midplane region, increasing $L_\parallel$ provides additional radiative volume. This effect is responsible for the significant enhancement of $K_{L_\parallel}$ shown in figure 2 for curves with a high shoulder (high temperature) region, particularly neon. The reason for both coronal and non-coronal argon curves behaving similarly is due to their curves converging at high temperature (not shown).

Term γ is a consequence of rearranging the equation to obtain the other terms. It captures the changes to the $q_\parallel$ profile above the X-point, which determines how much heat flux arrives in the divertor region that must be dissipated. This is manifested in figure 2 as a reduction in K_{f_R} and $K_{L_\parallel}$. In the case of K_{f_R}, increasing

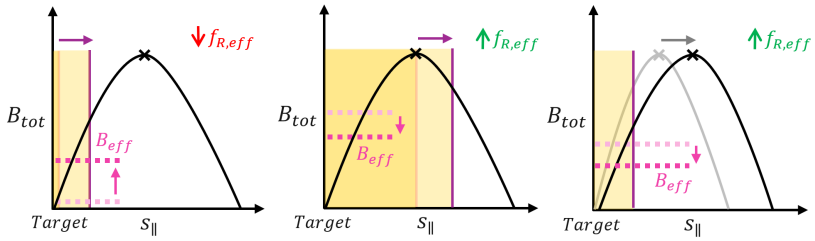

FIG. 3. Effects caused by term α due to the "radiation averaging" of the B field in an outer divertor. a) Broadening radiation below the X-point increases B_{eff}. b) Broadening radiation above the X-point can reduce B_{eff}. c) Increasing connection length reduces B_{eff}.

total flux expansion enhances divertor region radiation, leading to a lower proportion of radiation above the X-point. In the case of $K_{L_{\parallel}}$, greater $L_{\parallel}$ slightly shrinks the radiation region, reducing its proportion of the overall connection length, decreasing radiation above the X-point. In both cases, the reduced upstream radiation results in an increased heat flux at the X-point to dissipate and more difficult detachment access.

5. IMPACT ON DIVERTOR DESIGN

While separating f_R and $L_{\parallel}$ effects is valuable for first-principles analysis, in reality strike point movement results in both f_R and $L_{\parallel}$ changing simultaneously. To provide guidance on how the optimum changes with radiation width, the baseline DLS-Extended calculation was repeated for a grid of 150 different potential inner and outer strike point locations, resulting in a parameter space of f_R and $L_{\parallel}$. Each new magnetic profile was created by interpolating a new divertor leg in poloidal R,Z space, calculating a new parallel connection length by assuming constant B_{pol}/s_{pol}, recalculating B_{tor} assuming $B_{tor} \propto R^{-1}$ and finally computing $B = \sqrt{B_{tor}^2 B_{pol}^2}$. The region above the X-point was kept the same as the baseline design. The profiles were simulated in DLS-Extended to obtain the detachment threshold and detachment window for both the thin curve with no radiation effects, and the non-coronal argon curve which is most relevant to STEP. All settings were carried on from the baseline using the "match temperature" case to be as comparable as possible, and the results are shown in figure 4.

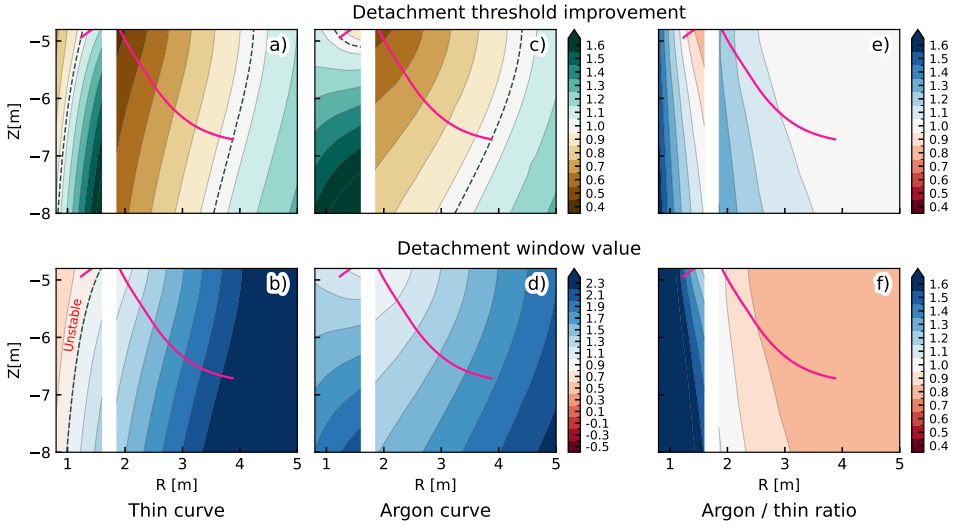

FIG. 4. Effect of moving the strike-point position on detachment performance with the thin cooling curve: a) Improvement to detachment threshold and b) the absolute value of the detachment window. This is repeated for the argon curve in c) and d), respectively, showing the impact of broadening radiation. The final column in e) and f) show the ratio of the argon to thin curve results for the detachment threshold improvement and detachment window value, respectively.

Both curves show weak sensitivity of the outer divertor to vertical movement, possibly allowing for a reduction in machine height without affecting detachment access. The argon curve makes the outer less sensitive to horizon-

tal movement, reducing the detachment access penalty of a vertical leg. The argon curve dramatically improves inner detachment front stability, eliminating the unstable zone. The outer is destabilised with a window reduction of 20%. Finally, The argon curve shows that the inner divertor would significantly benefit from a longer leg.

The effects of switching from the thin to the argon curve will be stronger for broader radiating impurities (e.g. neon) and weaken for narrower radiating species (e.g. nitrogen). They are caused by a combination of terms α, β, δ and γ described in section 4.2. They are dominated by the "averaging-out" radiation effect where the impact of B field variation is reduced, particularly for the inner, as shown in figure 2, as well as the $L_{\parallel}$ enhancement, primarily due to midplane radiation.

6. LIMITATIONS AND OUTLOOK

DLS-Extended offers a highly transparent, first-principles-based framework for estimating the influence of divertor magnetic configuration design on detachment access and sensitivity. Its simplicity, fast runtime (1-2s per front location) and minimal reliance on arbitrary or empirical tuning parameters make it particularly interpretable and a valuable tool for not just early-stage equilibrium design and magnetic geometry optimisation, but also first-principles studies like the one in the present work.

However, as with all reduced models, there are tradeoffs that require higher fidelity models to assess. The most significant is the lack of particle sinks and mechanisms for energy dissipation besides radiation. Cross-field transport, neutral reactions and even electron-ion equipartition can violate the constant pressure assumption [27]. The impact of cross-field transport due to localised particle sources can also be significant, but nevertheless allows a reasonable comparison to SOLPS given an appropriate field line choice. While the majority of the experimental and simulation studies described in section 4.1 recover the K_{f_R} and $K_{L_{\parallel}}$ in the thin radiation limit even in unseeded studies, which hints at a commonality between radiation and hydrogenic processes, neutral effects are important, e.g. through neutral closure, which was found to have a significant impact on the f_R benefit including through increased parallel flows [18, 31, 15]. Until reduced models are created to capture these effects, DLS-Extended and similar models are best used for tightly baffled devices which mitigate these effects.

The strong influence of radiation distribution on detachment found in the present work highlights the need for high-fidelity simulation and experimental studies of divertor magnetic design in the presence of seeded impurities. It also motivates work on local detachment sensitivity throughout the divertor leg, to build on the preliminary investigation only considering the detachment window. There is also a lot of promise in integrating DLS-Extended in other workflows, such as divertor design scoping and equilibrium design.

7. CONCLUSIONS

In this work, we introduced DLS-Extended, a new model which relaxes the infinitely thin radiation region assumption in the original DLS (Detachment Location Sensitivity) model [11, 4, 12], revealing a number of novel radiation-driven effects on detachment access and stability. To assess the accuracy of the radiation profiles, a baseline comparison to SOLPS-ITER simulations of an initial STEP design was conducted for both the inner and outer divertors, showing good agreement for the chosen SOL rings. The SOLPS simulations show broad radiation in both the inner and outer divertors.

In order to evaluate the impact of the radiation distribution, DLS-Extended was used to quantify the effect of increasing total flux expansion f_R and total parallel connection length $L_{\parallel}$ in the presence of a thin and a STEP-relevant argon cooling curve, finding that the f_R benefit weakens and the $L_{\parallel}$ benefit strengthens as the radiation broadens. The dominant mechanisms are the radiation "averaging-out" the B field along the divertor leg and reducing the overall impact of B field variation, and the presence of midplane radiation increasing radiating volume when the connection length is increased.

In a more realistic study, DLS-Extended was used to map a parameter space of strike point positions to evaluate the variation in detachment access and detachment window with and without a broad radiating curve. The results confirmed that B field variation effects were weakened, resulting in a dramatic improvement in inner detachment front stability and a moderate reduction in outer detachment front stability. Broad radiation reduces the sensitivity of both divertors to horizontal strike-point movement, while significantly increasing the sensitivity of the inner to vertical movement. This opens the possibility to refine the divertor design to better meet engineering and cost constraints, e.g. by lowering machine height, if confirmed by higher fidelity models.

Overall, the application of DLS-Extended to STEP divertor optimisation is a promising example of how divertor magnetic configuration design can be scoped at very low computational cost, either as part of reactor equilibrium design or a multi-fidelity exhaust modelling study. The results show optimisation potential in both the inner and outer divertor, and justify the need for further experimental and high-fidelity simulation studies to confirm the radiation effects.

ACKNOWLEDGEMENTS

The authors would like to thank Bruce Lipschultz for helpful discussions during this project.

This work was performed under the auspices of the U.S. Department of Energy by Lawrence Livermore National Laboratory under contract DE-AC52-07NA27344. This project was funded by EPSRC CDT in the Science and Technology of Fusion Energy, Grants EP/L01663X/1, EP/S022430/1.

REFERENCES

REFERENCES

[1] Hartmut Zohm. "Assessment of DEMO challenges in technology and physics". In: *Fusion Engineering and Design* 88.6-8 (2013), pp. 428–433.

[2] A Loarte et al. "Power and particle control". In: *Nuclear Fusion* 47.6 (2007), S203.

[3] A. Q. Kuang et al. "Divertor heat flux challenge and mitigation in SPARC". In: *Journal of Plasma Physics* 86.5 (2020), p. 865860505. DOI: 10.1017/S0022377820001117.

[4] C. Cowley et al. "Optimizing detachment control using the magnetic configuration of divertors". In: *Nuclear Fusion* 62.8 (July 2022), p. 086046. DOI: 10.1088/1741-4326/ac7a4c.

[5] Hendrik Meyer. "Plasma burn - Mind the gap". In: *Philosophical Transactions of the Royal Society A: Mathematical, Physical and Engineering Sciences* 382 (2280 Aug. 2024). ISSN: 1364503X. DOI: 10.1098/rsta.2023.0406.

[6] A. Kallenbach et al. "Impurity seeding for tokamak power exhaust: From present devices via ITER to DEMO". In: *Plasma Physics and Controlled Fusion* 55 (12 2013). ISSN: 07413335. DOI: 10.1088/0741-3335/55/12/124041.

[7] LL Lengyel. *Analysis of radiating plasma boundary layers*. Tech. rep. Max-Planck-Institut für Plasmaphysik, 1981.

[8] D. Moulton et al. "Comparison between SOLPS-4.3 and the Lengyel Model for ITER baseline neon-seeded plasmas". In: *Nuclear Fusion* 61 (4 Apr. 2021). ISSN: 17414326. DOI: 10.1088/1741-4326/abe4b2.

[9] A. E. Järvinen et al. "Parametric scaling of power exhaust in EU-DEMO alternative divertor simulations". In: *Nuclear Materials and Energy* 34 (Mar. 2023). ISSN: 23521791. DOI: 10.1016/j.nme.2023.101378.

[10] M. L. Reinke. "Heat flux mitigation by impurity seeding in high-field tokamaks". In: *Nuclear Fusion* 57 (3 2017). ISSN: 17414326. DOI: 10.1088/1741-4326/aa5145.

[11] Bruce Lipschultz, Felix I Parra, and Ian H Hutchinson. "Sensitivity of detachment extent to magnetic configuration and external parameters". In: *Nuclear Fusion* 56.5 (2016), p. 056007.

[12] O. Myatra et al. "Predictive SOLPS-ITER simulations to study the role of divertor magnetic geometry in detachment control in the MAST-U Super-X configuration". In: *Nuclear Fusion* 63 (9 Sept. 2023). ISSN: 17414326. DOI: 10.1088/1741-4326/acea33.

[13] C. Theiler et al. "Results from recent detachment experiments in alternative divertor configurations on TCV". In: *Nuclear Fusion* 57 (7 Mar. 2017). ISSN: 17414326. DOI: 10.1088/1741-4326/aa5fb7.

[14] H. Reimerdes et al. "TCV experiments towards the development of a plasma exhaust solution". In: *Nuclear Fusion* 57 (12 Sept. 2017). ISSN: 17414326. DOI: 10.1088/1741-4326/aa82c2.

[15] M. Carpita et al. "Parallel flows as a key component to interpret Super-X divertor experiments". In: *Nuclear Fusion* 64 (4 Apr. 2024). ISSN: 17414326. DOI: 10.1088/1741-4326/ad2a2a.

[16] R. Maurizio et al. "Divertor power load studies for attached L-mode single-null plasmas in TCV". In: *Nuclear Fusion* 58 (1 Jan. 2018). ISSN: 17414326. DOI: 10.1088/1741-4326/aa986b.

[17] B. Covele et al. "An exploration of advanced X-divertor scenarios on ITER". In: *Nuclear Fusion* 54 (7 2014). ISSN: 17414326. DOI: 10.1088/0029-5515/54/7/072006.

[18] T. W. Petrie et al. "Effect of changes in separatrix magnetic geometry on divertor behaviour in DIII-D". In: *Nuclear Fusion* 53 (11 Nov. 2013). ISSN: 00295515. DOI: 10.1088/0029-5515/53/11/113024.

[19] D. Brida et al. "Transport and profile broadening in the private flux region of ASDEX upgrade and role for power exhaust". In: *Nuclear Fusion* 65 (2 Feb. 2025). ISSN: 17414326. DOI: 10.1088/1741-4326/adac76.

[20] D. Moulton et al. “Super-X and conventional divertor configurations in MAST-U ohmic L-mode; a comparison facilitated by interpretative modelling”. In: *Nuclear Fusion* 64 (7 July 2024). ISSN: 17414326. DOI: 10.1088/1741-4326/ad4f9c.

[21] Kevin Verhaegh et al. “Divertor shaping with neutral baffling as a solution to the tokamak power exhaust challenge”. In: *Communications Physics* 8 (1 Dec. 2025). ISSN: 23993650. DOI: 10.1038/s42005-025-02121-1.

[22] D. Moulton et al. “Using SOLPS to confirm the importance of total flux expansion in Super-X divertors”. In: *Plasma Physics and Controlled Fusion* 59 (6 2017). ISSN: 13616587. DOI: 10.1088/1361-6587/aa6b13.

[23] A. Kallenbach et al. “Analytical calculations for impurity seeded partially detached divertor conditions”. In: *Plasma Physics and Controlled Fusion* 58 (4 2016). ISSN: 13616587. DOI: 10.1088/0741-3335/58/4/045013.

[24] A. Gallo et al. “Impact of the plasma geometry on divertor power exhaust: Experimental evidence from TCV and simulations with SolEdge2D and TOKAM3X”. In: *Plasma Physics and Controlled Fusion* 60 (1 Jan. 2018). ISSN: 13616587. DOI: 10.1088/1361-6587/aa857b.

[25] S. Wiesen et al. “The new SOLPS-ITER code package”. In: *Journal of Nuclear Materials* 463 (2015), pp. 480–484. ISSN: 00223115. DOI: 10.1016/j.jnucmat.2014.10.012. URL: http://dx.doi.org/10.1016/j.jnucmat.2014.10.012.

[26] R. T. Osawa et al. “Assessment of the impact of fuelling puff location on divertor impurity compression and enrichment in STEP”. In: *Nuclear Fusion* 64 (10 Oct. 2024). ISSN: 17414326. DOI: 10.1088/1741-4326/ad677a.

[27] Cyd Cowley. “Modelling of Alternative Divertor Power Exhaust”. PhD thesis. University of York, 2024.

[28] Lyman Spitzer and Richard Härm. “Transport Phenomena in a Completely Ionized Gas”. In: *Physical Review* 89 (5 Mar. 1953), pp. 977–981. ISSN: 0031-899X. DOI: 10.1103/PhysRev.89.977. URL: https://link.aps.org/doi/10.1103/PhysRev.89.977.

[29] FusionDLS Developers. *FusionDLS: Detachment Location Sensitivity*. https://github.com/FusionDLS/FusionDLS. Accessed: 2025-06-15. 2025.

[30] Thomas Body, Arne Kallenbach, and Thomas Eich. “A simple, accurate model for detachment access”. In: *Nuclear Fusion* 65 (8 Aug. 2025), p. 086002. ISSN: 0029-5515. DOI: 10.1088/1741-4326/ade4d9. URL: https://iopscience.iop.org/article/10.1088/1741-4326/ade4d9.

[31] A. Fil et al. “Separating the roles of magnetic topology and neutral trapping in modifying the detachment threshold for TCV”. In: *Plasma Physics and Controlled Fusion* 62 (3 2020). ISSN: 13616587. DOI: 10.1088/1361-6587/ab69bb.

[32] Peter C Stangeby et al. *The plasma boundary of magnetic fusion devices*. Vol. 224. Institute of Physics Pub. Philadelphia, Pennsylvania, 2000.

[33] R. J. Goldston, M. L. Reinke, and J. A. Schwartz. “A new scaling for divertor detachment”. In: *Plasma Physics and Controlled Fusion* 59 (5 Mar. 2017). ISSN: 13616587. DOI: 10.1088/1361-6587/aa5e6e.

[34] Tom Body, Christoph Hasse, and cfsjamie. *cfs-energy/radas: Zenodo release*. Version v2024.8.1. Nov. 2024. DOI: 10.5281/zenodo.14182360. URL: https://doi.org/10.5281/zenodo.14182360.